

Ba₆RE₂Ti₄O₁₇ (RE= Nd, Sm, Gd, Dy-Yb): A family of Rare-Earth-based layered triangular lattice magnets

Fangyuan Song,[†] Andi Liu,^{†,‡} Qiao Chen,[§] Jin Zhou,[†] Jingxin Li,[#] Wei Tong,[#] Shun Wang,[§] Yanhong Wang,^{||} Hongcheng Lu,^{||} Songliu Yuan,[†] Hanjie Guo,^{‡*} Zhaoming Tian^{†*}

[†] School of Physics and Wuhan National High Magnetic Field Center, Huazhong University of Science and Technology, Wuhan, 430074, China.

[‡] Songshan Lake Materials Laboratory, Dongguan, Guangdong 523808, China

[§] School of Physics and MOE Key Laboratory of Fundamental Physical quantum Physics, PGMF, Huazhong University of Science and Technology, Wuhan, 430074, China.

[#] Anhui Province Key Laboratory of Condensed Matter Physics at Extreme Conditions, High Magnetic Field Laboratory, Chinese Academy of Sciences, Hefei, 230031, China.

^{||}Key Laboratory of Material Chemistry for Energy Conversion and Storage, School of Chemistry and Chemical Engineering, Huazhong University of Science and Technology, Wuhan, 430074, China.

ABSTRACT: The exploration of new rare-earth (RE)-based triangular-lattice materials plays a significant role in motivating the discovery of exotic magnetic states. Herein, we report a family of hexagonal perovskite compounds Ba₆RE₂Ti₄O₁₇ (RE = Nd, Sm, Gd, Dy-Yb) with space group of *P6₃/mmc*, where magnetic RE³⁺ ions are distributed on the parallel triangular-lattice layers within the *ab*-plane and stacked in an “AA”-type fashion along the *c*-axis. The low-temperature magnetic characterizations indicate that all synthesized Ba₆RE₂Ti₄O₁₇ compounds exhibit the dominant antiferromagnetic (AFM) interactions and the absence of magnetic order down to 1.8 K. The isothermal magnetization and electron spin resonance results reveal the distinct magnetic anisotropy for the compounds with different RE ions. Moreover, the as-grown Ba₆Nd₂Ti₄O₁₇ single crystals exhibit the Ising-like magnetic anisotropy with magnetic easy-axis perpendicular to the triangle-lattice plane and no long-range magnetic order down to 80 mK, as the quantum spin liquid candidate with dominant Ising-type interactions.

■ INTRODUCTION

The triangular-lattice antiferromagnets have attracted great attention to search for the exotic magnetic states and emergent magnetic phenomena. One of archetypical case is the quantum spin liquid (QSL) state, which refers to a highly spin-entangled state but without magnetic order down to the lowest temperature. Since the initial theoretical proposal of QSL state in two-dimensional (2D) triangular-lattice Heisenberg antiferromagnets by P. W. Anderson,¹ significant research efforts have been made to realize this exotic state in real materials especially the antiferromagnetically coupled spin-1/2 triangular lattice systems. The typical examples for such states include the organic compounds κ -(BEDT-TTF)₂Cu₂(CN)₃, EtMe₂Sb[Pd(dmit)₂]₂ and inorganic NiGa₂S₄, Ba₃CuSb₂O₉ compounds.²⁻⁵ Additionally, the triangular-lattice antiferromagnets can exhibit exotic magnetism including the novel up-up-down (uud) ground state stabilized by quantum fluctuations and field-induced quantum phase transition behaviors, which is manifested by a one-third (1/3) fractional magnetization over a finite magnetic field range as experimentally confirmed in Cs₂CuBr₄ and

$\text{Na}_2\text{BaCo}(\text{PO}_4)_2$,^{6,7} as so on.

Compared to large numbers of studies on $S=1/2$ triangular-lattice magnets containing transition-metal (TM) ions, in past decade, the rare earth (RE)-based materials have also attracted a growing attention to explore the novel magnetic states. The large spin-orbit coupling and crystal electric field (CEF) effects of 4f electrons of RE ions can lead to highly anisotropic exchange interactions. For the compounds including Kramers ions with odd 4f electrons (like Ce^{3+} , Nd^{3+} , and Yb^{3+}), its low temperature magnetism can be well described by a spin-orbit coupled $J_{\text{eff}} = 1/2$ moments, thus provide the platform to realize the novel magnetic states beyond the 3d TM-based ones. Until now, several RE-based magnets with triangle lattice have been studied to search for the QSL states, such as YbMgGaO_4 ,⁸ AYbCh_2 ($A = \text{Li}^+$, Na^+ , K^+ , Cs^+ , $\text{Ch} = \text{O}$, S , Se ;) ⁹⁻¹² and $\text{PrZnAl}_{11}\text{O}_{19}$,¹³ etc. Moreover, some of compounds are interesting due to the observation of novel quantum magnetic phases like the Berezinskii-Kosterlitz-Thouless (BKT) phase in TmMgGaO_4 and spin glass phase in YbZnGaO_4 and quantum dipolar liquid in $\text{Yb}(\text{BaBO}_3)_3$ systems,¹⁴⁻¹⁶ etc. Meanwhile, the experimental identifications on the above exotic magnetic states remain to be controversial due to the unavoidable intrinsic antisite disorder, structural distortion and complex superexchange pathway in real materials.¹⁷ Based on this consideration, new scenarios on materials' design are required to explore the novel magnetic phases. In this respect, very recently, one route on realizing the QSL state based on the dominant Ising-type correlations instead of Heisenberg-type interactions has been experimentally investigated on triangular-lattice $\text{NdTa}_7\text{O}_{19}$,¹⁸ which is instructive to search for the novel magnetic states but limited materials have been identified. From the structure viewpoint, the stacking order of triangular-lattice multilayers as well as the formation of bilayer structure have been proposed to introduce the magnetic frustration and generate diverse exotic magnetic states.^{19,20} Therefore, designing new RE-triangular-lattice materials with different stacking structures and magnetic anisotropy are highly desirable to enrich the exotic magnetic phenomena.

In this work, we report a family of RE-based triangular lattice compounds $\text{Ba}_6\text{RE}_2\text{Ti}_4\text{O}_{17}$ ($\text{RE} = \text{Nd}$, Sm , Gd , Dy - Yb) crystallized into the hexagonal crystal structure (space group $P6_3/mmc$). Among the family, two members $\text{Ba}_6\text{RE}_2\text{Ti}_4\text{O}_{17}$ ($\text{RE}=\text{Nd}$, Y) have been synthesized and structurally characterized to be the 12-layer hexagonal perovskite structure by X-ray and neutron powder diffractions.²¹ While, the lattice geometry of magnetic RE^{3+} ions and their magnetism have not been unveiled, motivating the present study. Here, on the basis of structure analysis, we reveal that magnetic RE^{3+} ions form the parallel triangular-lattice layers with "AA"-type stacking fashion along the c -axis and the neighboring interlayer magnetic planes are separated alternatively by the nonmagnetic Ti_2O_9 dimers and double sheets of TiO_4 tetrahedra. For all $\text{Ba}_6\text{RE}_2\text{Ti}_4\text{O}_{17}$ compounds, magnetic measurements and electron spin resonance (ESR) spectra indicate the dominant antiferromagnetic (AFM) exchange interactions and absence of magnetic order down to 1.8 K. Moreover, the $\text{Ba}_6\text{Nd}_2\text{Ti}_4\text{O}_{17}$ single crystals have been successfully grown and which exhibit the Ising-like anisotropy with easy magnetization along the c -axis and no long-range magnetic order down to 0.08 K.

■ EXPERIMENTAL SECTION

Material Synthesis. The series of $\text{Ba}_6\text{RE}_2\text{Ti}_4\text{O}_{17}$ ($\text{RE} = \text{Nd}$, Sm - Gd , Dy - Yb) polycrystals were synthesized by the conventional solid-state reaction using the BaCO_3 (99.9%), TiO_2 (99.9%) and RE oxides ($\text{RE}=\text{Nd}$, Sm - Gd ,

Dy-Yb, 99.9%) as starting materials. No uncommon hazards are noted in the experiment on sample synthesis. The RE oxides were dried at 800 °C overnight prior to use. The stoichiometric mixtures of the raw materials were thoroughly ground for two hours, pressed into pellets and preheated at 1100 °C for 24 h. For Ba₆RE₂Ti₄O₁₇ (RE = Nd, Sm-Gd) samples, the products were reground and calcined in air at temperature regions from 1250 to 1300 °C for 4 days. For RE = Dy-Yb samples, the higher reacting temperatures of 1350 -1400 °C are required to obtain the pure phase sample. All the synthesized Ba₆RE₂Ti₄O₁₇ samples are stable in air, and the optical images of the Ba₆RE₂Ti₄O₁₇ pellets are shown in Figure S1 (see supporting information).

The Ba₆Nd₂Ti₄O₁₇ single crystal was grown by high-temperature flux method using BaCl₂ as flux, similar to the previous descriptions.²² The mixtures of Ba₆Nd₂Ti₄O₁₇ polycrystalline powders and BaCl₂ flux with a ratio of 1:15 were placed in a 50-ml platinum crucible and then heated to 1250 °C for 24 hours to ensure the homogeneous melting. Then, the temperature of furnace was cooled slowly to 800 °C at the rate of 3 °C /h, and finally cooled down to room temperature. The Ba₆Nd₂Ti₄O₁₇ single crystals were separated by dissolving the BaCl₂ flux in hot water. The as-grown Ba₆Nd₂Ti₄O₁₇ single crystal has the hexagonal shape, as shown in the inset of Figure 1a.

Structure Characterization. The crystal structure and phase purity of Ba₆RE₂Ti₄O₁₇ (RE = Nd, Sm, Eu, Gd, Dy-Yb) compounds were analyzed by Powder X-ray diffraction (PXRD, SmartLab) data at room temperature with CuK_α ($\lambda = 1.5418 \text{ \AA}$). The structural refinements for Ba₆RE₂Ti₄O₁₇ were carried out by Rietveld method with the GSAS program. The diffraction data of Ba₆Nd₂Ti₄O₁₇ single crystals were examined by single-crystal X-ray diffraction (SXRD) using a Bruker SMART APEX DUO diffractometer equipped with a CCD detector (graphite-monochromated MoK_α radiation, $\lambda = 0.71073 \text{ \AA}$). The structure was refined by the ShelXL least squares software package with the Olex2 program.

Physical Property Measurements. Magnetic properties were measured with a commercial superconducting quantum interference device (SQUID, Quantum Design) magnetometer. The dc magnetic susceptibilities $\chi(T)$ of Ba₆RE₂Ti₄O₁₇ polycrystals were measured under applied field of 1 kOe in temperature range from 1.8 to 300 K. The isothermal magnetization $M(\mu_0H)$ measurements were collected by SQUID with field up to 7 T. Low-temperature X-band electron paramagnetic resonance (EPR) spectra at a microwave frequency of 9.4 GHz were carried out using a Bruker spectrometer equipped with an Oxford ESR910 liquid helium cryostat. The specific heat $C_p(T)$ measurements of Ba₆Nd₂Ti₄O₁₇ compounds were performed using a Quantum Design physical properties measurement system (PPMS) in the temperature range 2 - 150 K at different magnetic fields. At low temperatures down to 0.08 K, the specific heat was measured using the PPMS equipped with a dilution refrigeration by the heat capacity option.

■ RESULTS AND DISCUSSION

Structure Description. The synthesized Ba₆RE₂Ti₄O₁₇ (RE = Nd, Sm, Gd, Dy-Yb) polycrystalline samples are isostructural and crystalized into the hexagonal crystal structure with space group $P6_3/mmc$ (No.194). Figure 1a shows the experimental and the refined XRD patterns for the selected Ba₆RE₂Ti₄O₁₇ (RE = Nd, Sm, Ho) samples. Here, the crystal structure of Ba₆Y₂Ti₄O₁₇ was adopted as an initial model for Rietveld refinement,²¹ the refinements yield a good fit to the observed experimental data. The obtained lattice parameters and atomic

positions of $\text{Ba}_6\text{RE}_2\text{Ti}_4\text{O}_{17}$ samples are listed in Table S1 (see supporting information). As reduced RE^{3+} ionic radii, both the lattice constants (a , c) and unit-cell volume (V) follow a monotonically decrease (see Figure 1b, c). The selected bond distances, bond angles and intralayer and interlayer RE-RE distances for $\text{Ba}_6\text{RE}_2\text{Ti}_4\text{O}_{17}$ polycrystals are summarized in Table 1. For the grown $\text{Ba}_6\text{Nd}_2\text{Ti}_4\text{O}_{17}$ single crystals, the refined crystallographic data is presented in Table 2.

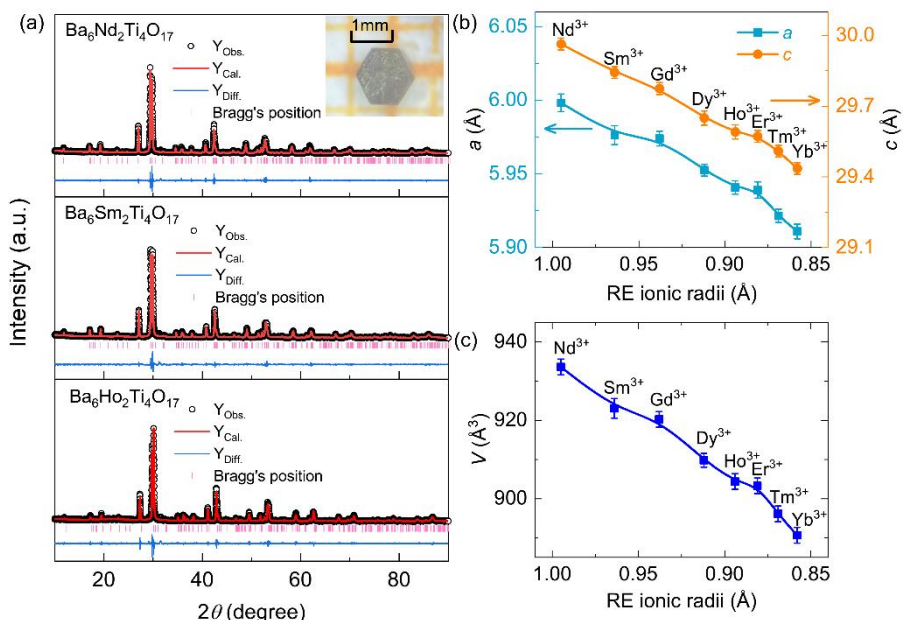


Figure 1. (a) The experimental and refined powder X-ray diffraction (XRD) patterns of $\text{Ba}_6\text{RE}_2\text{Ti}_4\text{O}_{17}$ (RE = Nd, Sm, Ho) compounds, the experimental data is shown by black open circles, the refined data is in red line and the difference in blue line. Inset shows the photograph of as-grown $\text{Ba}_6\text{Nd}_2\text{Ti}_4\text{O}_{17}$ single crystal on 1 mm graph paper. (b) The variation of lattice constants and (c) the unit-cell volume versus RE ionic radii of $\text{Ba}_6\text{RE}_2\text{Ti}_4\text{O}_{17}$.

Table 1. Some bond distances, bond angles, and RE-RE distances of polycrystalline $\text{Ba}_6\text{RE}_2\text{Ti}_4\text{O}_{17}$ (RE = Nd, Sm, Gd, Dy-Yb).

RE	Nd	Sm	Gd	Dy	Ho	Er	Tm	Yb
REO ₆								
RE-O ₂ ×3	2.377(5)	2.371(2)	2.296(2)	2.341(1)	2.231(9)	2.263(3)	2.375(2)	2.232(7)
RE-O ₃ ×3	2.325(0)	2.259(5)	2.244(2)	2.142(3)	2.224(6)	2.167(1)	2.175(5)	2.244(5)
Average RE-O	2.351(2)	2.315(3)	2.270(2)	2.241(7)	2.228(3)	2.215(2)	2.275(4)	2.238(6)
Interplane RE-RE (Å)								
	7.547(2)	7.411(2)	7.370(3)	7.352(2)	7.323(0)	7.319(5)	7.307(5)	7.301(7)
	7.434(5)	7.510(3)	7.516(8)	7.449(5)	7.472(1)	7.466(2)	7.446(8)	7.416(0)
intraplane RE-RE (Å)								
	5.998(2)	5.976(2)	5.974(0)	5.952(5)	5.940(7)	5.939(0)	5.921(6)	5.910(9)
O ₂ -RE-O ₃ (deg)	95.5(1)	94.4(2)	94.6(5)	89.3(8)	94.7(7)	94.7(7)	93.2(1)	95.9(5)
Ti(1)O ₄								
Ti(1)-O ₁ ×1	1.654(9)	1.720(4)	1.746(2)	1.50(4)	1.866(7)	1.689(6)	1.745(5)	1.806(0)
Ti(1)-O ₂ ×3	1.808(4)	1.762(5)	1.835(2)	1.758(2)	1.840(2)	1.813(1)	1.691(4)	1.820(7)

Average Ti(1)-O	1.770(0)	1.751(9)	1.812(8)	1.694(6)	1.846(8)	1.782(2)	1.704(9)	1.817(0)
O ₁ -Ti-O ₂ (deg)	108.4(8)	109.6(3)	108.5(9)	112.4(8)	110.7(9)	109.1(4)	108.7(0)	106.2(6)
Ti(2)O ₆								
Ti(2)-O ₃ ×3	1.862(6)	1.928(4)	1.928(2)	2.140(3)	1.936(0)	1.974(7)	1.943(8)	1.873(5)
Ti(2)-O ₄ ×3	1.990(7)	1.960(0)	1.985(1)	1.947(2)	2.033(2)	1.995(5)	1.961(4)	1.994(8)
Average Ti(2)-O	1.926(7)	1.944(2)	1.956(7)	2.043(8)	1.984(6)	1.985(1)	1.952(6)	1.934(2)
O ₃ -Ti(2)-O ₄ (deg)	93.4(4)	93.6(4)	92.8(6)	95.3(8)	90.5(0)	91.9(7)	93.9(9)	91.4(2)
Ba(1)O ₆								
Ba(1)-O ₂ ×6	2.780(3)	2.836(8)	2.836(2)	2.902(2)	2.866(1)	2.835(1)	2.847(6)	2.775(1)
Average Ba(1)-O	2.780(3)	2.836(8)	2.836(2)	2.902(2)	2.866(1)	2.835(1)	2.847(6)	2.775(1)
O ₂ -Ba(1)-O ₂ (deg)	65.9(7)	66.2(6)	63.7(7)	65.5(6)	62.1(8)	63.2(1)	67.0(6)	62.6(1)
Ba(2)O ₁₀								
Ba(2)-O ₁ ×1	2.569(1)	2.515(7)	2.498(2)	2.673(3)	2.407(9)	2.594(2)	2.544(3)	2.545(2)
Ba(2)-O ₂ ×6	3.036(5)	3.019(5)	3.011(9)	2.994(0)	2.988(5)	2.991(7)	2.996(1)	2.985(5)
Ba(2)-O ₃ ×3	2.948(1)	2.934(3)	2.935(2)	2.76(4)	2.959(4)	2.934(2)	2.848(5)	2.912(0)
Average Ba(2)-O	2.963(2)	2.943(6)	2.937(5)	2.892(9)	2.921(7)	2.934(7)	2.906(6)	2.919(4)
O ₁ -Ba(2)-O ₃ (deg)	81.0(4)	81.8(5)	82.6(4)	84.0(3)	83.7(3)	83.0(0)	81.4(3)	81.8(9)
O ₁ -Ba(2)-O ₃ (deg)	147.7(4)	146.5(4)	146.2(4)	144.8(7)	145.9(6)	144.9(1)	144.9(4)	146.1(7)
O ₂ -Ba(2)-O ₃ (deg)	71.1(3)	69.6(2)	68.3(5)	66.3(6)	66.9(3)	59.5(6)	68.9(3)	68.6(4)
Ba(3)O ₉								
Ba(3)-O ₃ ×6	3.030(7)	3.023(2)	3.019(4)	3.060(9)	2.993(3)	2.999(0)	2.993(1)	2.975(9)
Ba(3)-O ₄ ×3	2.807(5)	2.794(9)	2.776(1)	2.644(2)	2.710(2)	2.759(9)	2.811(8)	2.767(0)
Average Ba(3)-O	2.926(3)	2.947(1)	2.938(3)	2.922(0)	2.898(9)	2.919(3)	2.932(7)	2.906(3)
O ₃ -Ba(3)-O ₄ (deg)	57.3(1)	58.1(7)	58.3(5)	58.8(2)	59.0(1)	59.2(6)	58.8(4)	57.5(5)
Ba(4)O ₁₂								
Ba(4)-O ₃ ×6	3.012(4)	3.007(6)	2.985(2)	3.17(4)	2.918(2)	2.941(8)	2.994(6)	2.914(6)
Ba(4)-O ₄ ×6	3.012(5)	3.002(1)	2.998(6)	2.979(7)	2.974(9)	2.979(1)	2.975(3)	2.965(7)
Average Ba(4)-O	3.012(4)	3.004(9)	2.991(9)	3.076(9)	2.9465(5)	2.960(4)	2.984(9)	2.940(2)
O ₃ -Ba(4)-O ₄ (deg)	55.3(9)	56.3(1)	56.5(4)	58.8(2)	57.1(6)	57.6(5)	62.0(5)	56.2(1)

Table 2. Crystal data and structure refinements of Ba₆Nd₂Ti₄O₁₇ single crystal.

Empirical formula	Ba ₆ Nd ₂ Ti ₄ O ₁₇
Formula weight	1576.12
T (K)	296
λ (Å)	0.711073
Space group	P6 ₃ /mmc
a (Å)	5.9934(10)
b (Å)	5.9934(10)
c (Å)	29.952(5)
α (°)	90

β (°)	90
γ (°)	120
V (Å ³)	931.8(3)
Z	2
Density (g cm ⁻³)	5.618
Absorption coefficient (mm ⁻¹)	19.596
GOF on F^2	1.256
R_1	0.0814
$wR_2 [I > 2 \sigma(I)]^a$	0.1436

Considering that all family members of Ba₆RE₂Ti₄O₁₇ (RE=Nd-Yb) share the same crystal structure, as a representative, the schematic crystal structure of Ba₆Nd₂Ti₄O₁₇ is presented in Figure 2a. The framework of crystal structure is constructed by the corner-sharing connections of distorted NdO₆ octahedron with the TiO₄ tetrahedra and face-sharing Ti₂O₉ bioctahedra. Within the *ab* plane, magnetic Nd³⁺ ions are occupied on a perfect triangular lattice with an equilateral nearest-neighboring Nd³⁺-Nd³⁺ intralayer distance of $a = 5.993(4)$ Å, then the triangular-lattice planes are stacked with an “AA”-type sequence along the crystallographic *c* axis with two different interlayer distances as shown in Figure 2b. Further checking the connections for the Nd³⁺ ions within the triangular-lattice plane, the adjacent NdO₆ octahedra are linked to each other by corner-sharing TiO₄ tetrahedra and TiO₆ octahedra and there exist two different Nd-O-Ti-O-Nd superexchange routes, as shown in Figure 2c. It is noteworthy that the intralayer Nd³⁺-Nd³⁺ distance $d_0 = a = 5.993(4)$ Å of Ba₆Nd₂Ti₄O₁₇ is just between ~ 6.224 Å of triangular-lattice antiferromagnet NdTa₇O₁₉¹⁸ and ~ 5.593 Å for triangular-lattice NdMgAl₁₁O₁₉,¹¹ then the intraplane exchange interactions of Ba₆Nd₂Ti₄O₁₇ should have comparable exchange interactions with the above two systems. Along the *c*-axis, the Nd³⁺ planes are well separated by the nonmagnetic layers constructed by Ti-O/Ba-O polyhedra, but the superexchange pathways are different for the alternative Nd³⁺ triangular layers. For the neighboring two Nd³⁺ layers with distance $d_1 = 7.426(3)$ Å, the interplane superexchange pathway are realized via the Ti₂O₉ dimers with the Nd-O-Ti-O-Ti-O-Nd bridges. While for the neighboring Nd³⁺ layers with distance $d_2 = 7.549(7)$ Å, they are separated by double sheets of TiO₄ tetrahedra, as illustrated in Figure 1c and Figure S2b. Accordingly, the Nd-Nd connections are realized through the “...Nd-Ti₂O₉-Nd-TiO₄/TiO₄-Nd-Ti₂O₉-Nd...” pathways along the *c*-axis. Further considering that the magnetic exchange interactions depend on their superexchange pathway, the interlayer exchange interactions between the neighboring Nd-Nd layers with space separation of d_2 are much smaller than to the ones with distance of d_1 , due to the absence of co-sharing oxygen atoms between the double sheets of TiO₄ tetrahedra (see Figure S2b in supporting information), which breaks the equivalency of interlayer exchange interactions for the alternative neighboring Nd³⁺ triangular layers. Thus, Ba₆Nd₂Ti₄O₁₇ compound can be regarded as the layered triangular lattice system with two alternative interlayer magnetic exchange interactions.

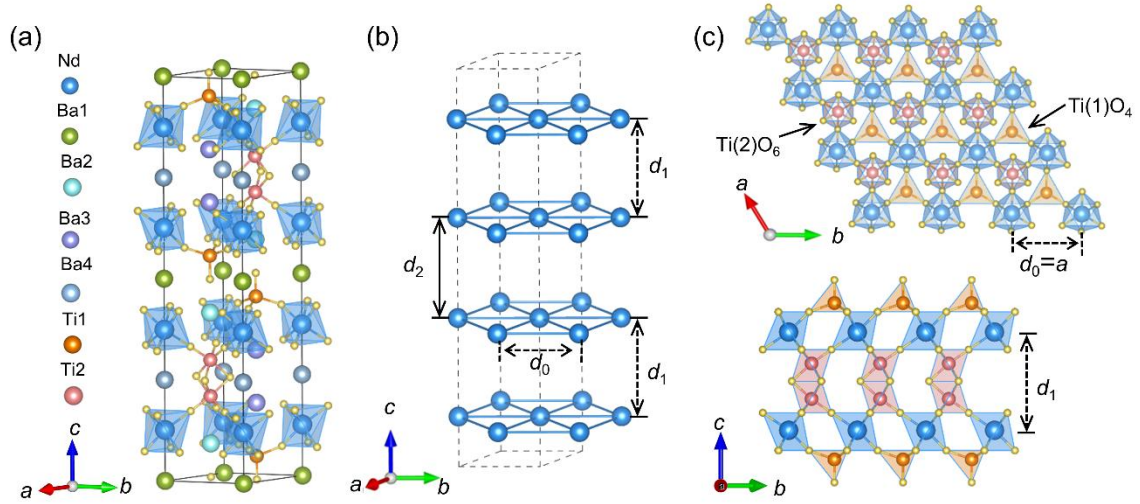


Figure 2. (a) The schematic crystal structure of $\text{Ba}_6\text{Nd}_2\text{Ti}_4\text{O}_{17}$ in the unit cell. (b) The lattice geometry of magnetic Nd^{3+} triangular-lattice planes and its stacking sequence along the c -axis, the in-plane distance of Nd^{3+} ions is denoted by d_0 and the interplanar distances are denoted by d_1 and d_2 . (c) Top view (upper panel) and side view (lower panel) of the NdO_6 octahedra with the connections of TiO_4 and TiO_6 groups.

The unit cell of $\text{Ba}_6\text{Nd}_2\text{Ti}_4\text{O}_{17}$ consists of eleven crystallographic sites: one Nd atom (Wyckoff site $4e$), four Ba atoms (Wyckoff site $2a$, $2b$, and $4f$), two Ti atoms (Wyckoff site $4f$), and four O atoms (Wyckoff site $4f$, $6h$, and $12k$), the detailed coordination environments of Nd, Ti1, Ti2, Ba1, Ba2, Ba3, Ba4 with surrounding oxygen atoms are depicted in Figure S1a. The local coordinate environment of NdO_6 octahedra has point group symmetry D_{3d} analogous to the case of KCeO_2 and NaYbO_2 .^{23,24} Based on the structure analysis of $\text{Ba}_6\text{Nd}_2\text{Ti}_4\text{O}_{17}$ single crystal, no antisite occupancy between the magnetic Nd^{3+} ions and non-magnetic $\text{Ba}^{2+}/\text{Ti}^{4+}$ cations in $\text{Ba}_6\text{Nd}_2\text{Ti}_4\text{O}_{17}$ are detected, which can be due to the significant difference of ionic radii of 0.983 Å, 1.35 Å and 0.605 Å for Nd^{3+} , Ba^{2+} and Ti^{4+} ions as well as their different coordination environments. For other $\text{Ba}_6\text{RE}_2\text{Ti}_4\text{O}_{17}$ samples, the structure refinements reveal only a tiny amount (0.06%–1.57%) of RE/Ti site disorder in our $\text{Ba}_6\text{RE}_2\text{Ti}_4\text{O}_{17}$ (RE = Sm, Gd, Dy-Yb) polycrystalline samples, suggests the weak antisite disorder for $\text{Ba}_6\text{RE}_2\text{Ti}_4\text{O}_{17}$ compounds. This weak disorder is attractive to investigate the intrinsic magnetism from the perfect triangular lattice of RE^{3+} moments.

Magnetic Properties of $\text{Ba}_6\text{RE}_2\text{Ti}_4\text{O}_{17}$. Magnetic susceptibility $\chi(T)$ measurements for the $\text{Ba}_6\text{RE}_2\text{Ti}_4\text{O}_{17}$ samples were carried out in temperature range from 1.8 K to 300 K under field of $\mu_0 H = 0.1$ T, the results are presented in Figure 3. The inverse susceptibility $1/\chi(T)$ is fitted by the Curie–Weiss (CW) law $1/\chi = (T - \theta_{\text{CW}})/C$, where C is the Curie Constant, θ_{CW} is the CW temperature. The effective moment μ_{eff} is calculated by $\mu_{\text{eff}} = (3k_B C/N_A)^{1/2}$, where k_B is the Boltzmann constant and N_A is Avogadro’s constant. Considering that the thermal population of electrons occupied on different crystal electric field (CEF) levels are dependent on the temperature, the CW fits are performed at both high-temperature ($T = 120$ –300 K) and low-temperature ($T = 5$ –10 K) regions, respectively. The $\chi^{-1}(T)$ data and CW fitting at low temperature regions are presented in Figure S3. The obtained θ_{CW} and μ_{eff} from the CW fits are summarized in Table 3. As shown in Figure 4, the isothermal field-dependent magnetizations $M(\mu_0 H)$ at different temperatures were fitted with the Brillouin

function $B_J(x) = \frac{2J_{\text{eff}}+1}{2J_{\text{eff}}} \coth \frac{2J_{\text{eff}}+1}{2J_{\text{eff}}} x - \frac{1}{2J_{\text{eff}}} \coth \frac{x}{2J_{\text{eff}}}$, where $x = g_J \mu_B J_{\text{eff}} \mu_0 H / k_B T$, J_{eff} is the effective angular momentum, g_J is the Lande's factor, and μ_B is the Bohr magneton. To perform the Brillouin function fits, the values of J_{eff} are fixed on the $M(\mu_0 H)$ curves at different temperatures for $\text{Ba}_6\text{RE}_2\text{Ti}_4\text{O}_{17}$ (RE=Nd, Gd, Dy, Ho, Er, Yb), the g -factor is used as adjusting parameter to fit the experimental data. Additionally, the Lande g -factors for some of compounds are determined based on the X-band electron spin resonance (ESR) results using $g_J = h \nu / \mu_B H_r$ (h is Plank's constant; $\nu = 9.4$ GHz is the microwave frequency; H_r is the resonance field). The elementary magnetic properties for $\text{Ba}_6\text{RE}_2\text{Ti}_4\text{O}_{17}$ are described separately as below.

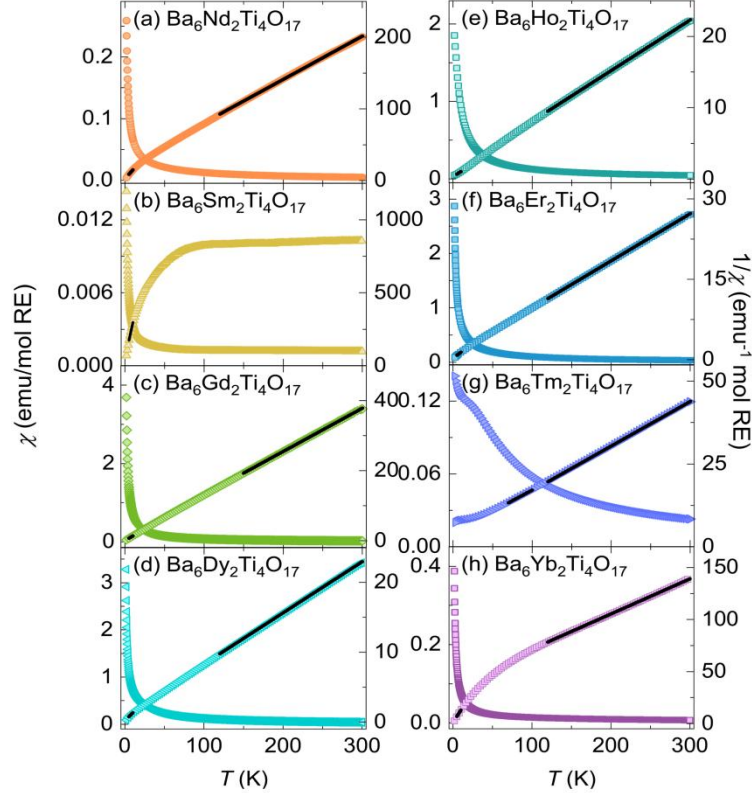


Figure 3. Temperature dependence of magnetic susceptibility $\chi(T)$ and inverse susceptibility $\chi^{-1}(T)$ measured at $\mu_0 H = 0.1$ T for $\text{Ba}_6\text{RE}_2\text{Ti}_4\text{O}_{17}$ (RE = Nd, Sm, Gd, Dy-Yb), respectively. The black solid lines show the Curie-Weiss fitting in high temperature and low temperature regimes.

Ba₆Nd₂Ti₄O₁₇. Figure 3a shows the magnetic susceptibility $\chi(T)$ curve of $\text{Ba}_6\text{Nd}_2\text{Ti}_4\text{O}_{17}$, no magnetic order is detected with temperature down to 1.8 K. The CW fits on $\chi^{-1}(T)$ at high temperatures yield CW temperature $\theta_{\text{cw}} = -33.7$ K and effective moment $\mu_{\text{eff}} = 3.64 \mu_B/\text{Nd}^{3+}$. This magnetic moment is consistent with the expected value $g_J[J(J+1)]^{1/2} = 3.62 \mu_B/\text{Nd}^{3+}$ for free Nd^{3+} ($4f^3, 4I_{9/2}$) ions. As decreased temperatures, magnetic contribution from the electrons at excited CEF levels is reduced which can be responsible for the variation of the slope of $\chi^{-1}(T)$ curve. The low-temperature fits give $\theta_{\text{cw}} = -1.74$ K and $\mu_{\text{eff}} = 2.50 \mu_B/\text{Nd}^{3+}$. The smaller μ_{eff} is expected due to the CEF effect, where more population of electrons will occupy on the lowest-lying Kramers doublet states at the low temperatures.²⁵ The magnetization $M(\mu_0 H)$ curves of $\text{Ba}_6\text{Nd}_2\text{Ti}_4\text{O}_{17}$ at different temperatures are depicted in Figure 4a. The experimental saturated magnetization $M_S \sim 1.25 \mu_B/\text{Nd}$ at 2 K is

close to half value of the effective magnetic moment, similar to the report in other Nd³⁺-based oxides.²⁵⁻²⁷ The fitting of the Brillouin function for magnetization curves at 2 K gives a good fit with the experimental data, which is due to the weak magnetic exchange interactions between Nd³⁺ moments.

Ba₆Sm₂Ti₄O₁₇. The susceptibility $\chi(T)$ of Ba₆Sm₂Ti₄O₁₇ is shown in Figure 3b. At high temperatures, it exhibits a temperature independent Van Vleck contribution from Sm³⁺ ($4f^5, ^6H_{5/2}$) ions as report in many Sm-containing compounds.^{26,28} Thus, the CW fitting is y performed at low temperatures between 5 and 10 K, which results in $\mu_{\text{eff}} = 0.567 \mu_{\text{B}}/\text{Sm}$ and $\theta_{\text{CW}} = -1.98 \text{ K}$, respectively. The negative θ_{CW} indicates the antiferromagnetic interactions between Sm³⁺ moments. The μ_{eff} value is smaller than the value $0.83 \mu_{\text{B}}/\text{Sm}$ of free ion but similar to the ones reported in Sm³⁺-containing oxides, such as Sm₃Sb₃Mg₂O₁₄ ($0.53 \mu_{\text{B}}/\text{Sm}$) and Sm₂Zr₂O₇ ($0.50 \mu_{\text{B}}/\text{Sm}$).^{26,28} The reduced moments in these compounds may be related to the CEF splitting of $J = 5/2$ multiplet of Sm³⁺ ions. The field-dependent magnetization $M(\mu_0H)$ at 2 K shows a nearly field dependence without magnetic saturation up to $\mu_0H = 7 \text{ T}$ (see Figure 4b).

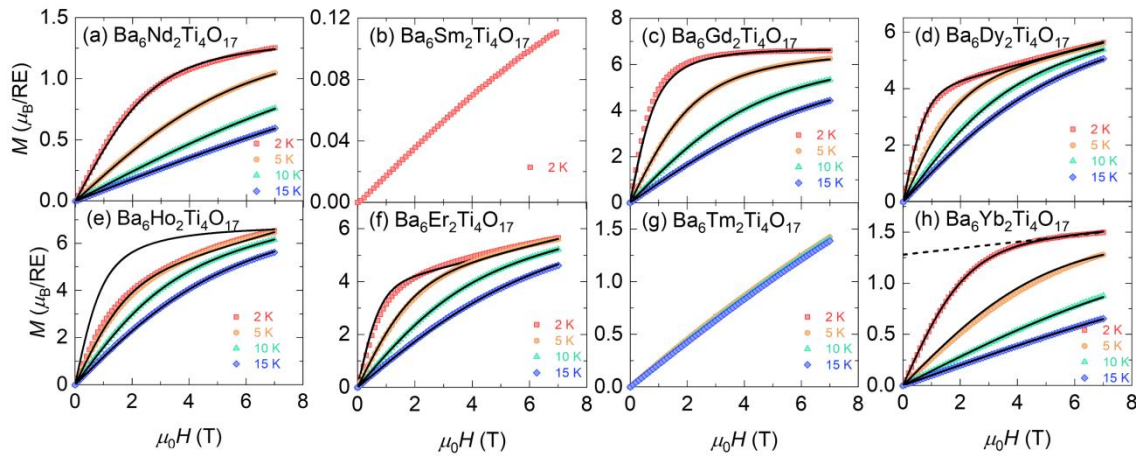


Figure 4. The isothermal field-dependent magnetization $M(\mu_0H)$ curves at different temperatures for Ba₆RE₂Ti₄O₁₇ (RE = Nd, Sm, Gd, Dy-Yb), the black solid lines show the fitted curves by Brillouin function.

Ba₆Gd₂Ti₄O₁₇. The $\chi(T)$ of Ba₆Gd₂Ti₄O₁₇ is shown in Figure 3c, which doesn't show any long-range magnetic order down to 1.8 K. High temperature CW fitting of $1/\chi(T)$ yields $\theta_{\text{CW}} = -6.4 \text{ K}$ and $\mu_{\text{eff}} = 8.05 \mu_{\text{B}}$, the fitted μ_{eff} is consistent with the value of $g_{\text{J}}[J(J + 1)]^{1/2} = 7.94 \mu_{\text{B}}/\text{Gd}^{3+}$ for the free Gd³⁺ ($4f^7, S=7/2, L=0$) ions. The low-temperature fitting gives $\theta_{\text{CW}} = -0.276 \text{ K}$ and $\mu_{\text{eff}} = 7.69 \mu_{\text{B}}/\text{Gd}^{3+}$, here the negative θ_{CW} value indicates the antiferromagnetic interactions between Gd³⁺ ions. The $M(\mu_0H)$ curves of Ba₆Gd₂Ti₄O₁₇ at 2 K display a nonlinear field dependence behavior and reaches saturation at field ~4 T with $M_{\text{S}} \sim 6.61 \mu_{\text{B}}$ (Figure 4c), which is close to the saturated magnetization $M_{\text{sat}} = g_{\text{J}}\mu_{\text{B}} = 7\mu_{\text{B}}/\text{Gd}^{3+}$ of Gd³⁺ moments with Heisenberg anisotropy of Gd³⁺ spins. The Brillouin function gives the well-matched fits to the experimental $M(\mu_0H)$ data using $J_{\text{eff}} = 7/2$, indicative of the dominant paramagnetic behaviors at 2 K. From the ESR spectra shown in Figure 5a, single resonance lines can be identified in the measured temperature regions. As temperature decreases from 50 K to 2 K, the g -factor shows a gradual increase from ~2.07 to ~2.49 as shown in Figure 6a, possibly due to the development of short-range AFM correlations.

Ba₆Dy₂Ti₄O₁₇. Figure 3d shows the $\chi(T)$ curve of Ba₆Dy₂Ti₄O₁₇. The high temperature CW fits yield $\theta_{\text{CW}} = -13.3$ K and $\mu_{\text{eff}} = 10.4 \mu_{\text{B}}/\text{Dy}$, this moment is close to $10.6 \mu_{\text{B}}/\text{Dy}$ of free Dy³⁺ (⁶H_{15/2}) ions. At low temperatures, linear fit on $\chi^{-1}(T)$ gives $\mu_{\text{eff}} = 8.49 \mu_{\text{B}}/\text{Dy}$ and $\theta_{\text{CW}} = -1.85$ K. The negative θ_{CW} indicates AFM couplings between local Dy³⁺ spins. Figure 4d shows the $M(\mu_0 H)$ curves at different temperatures. At 2 K, the magnetization shows nonlinear field dependence at field below 1.5 T and has linear field dependence at higher fields, which can be possibly from the Van Vleck magnetic contribution. By including a linear-field contribution into the Brillouin function, we can well fit the experimental $M(\mu_0 H)$ curves. The maximum magnetization value M_{sat} is $5.63 \mu_{\text{B}}/\text{Dy}$ in an applied field of $\mu_0 H = 7$ T, which is close to half of the expected Dy³⁺ saturation magnetization of $g_J \mu_{\text{B}} = 10 \mu_{\text{B}}/\text{Dy}^{3+}$ with Ising-like magnetic anisotropy. From the ESR spectra measured at different temperatures (see Figure 5b), the calculated g -factors increase and reach the values of 6.3- 6.7 as temperature is below 5 K, as presented in Figure 6b.

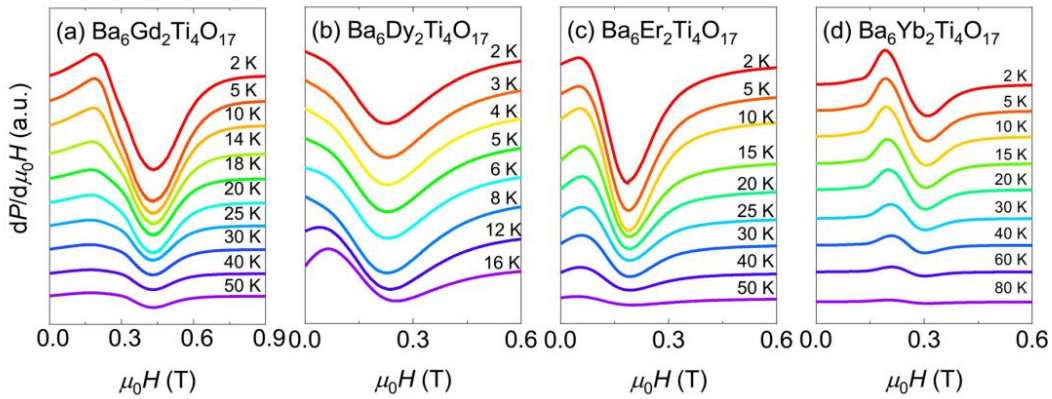


Figure 5. The ESR spectra at selected temperatures for Ba₆RE₂Ti₄O₁₇ (RE = Gd, Dy, Er, Yb) compounds with (a) RE = Gd, (b) RE = Dy, (c) RE = Er, (d) RE = Yb.

Ba₆Ho₂Ti₄O₁₇. As displayed in Figure 3e, the $\chi(T)$ curve of Ba₆Ho₂Ti₄O₁₇ does not show any hints of long-range magnetic order down to 1.8 K. The temperature-dependent susceptibility is similar to the one of Ba₆Dy₂Ti₄O₁₇. The high temperature CW fits give $\mu_{\text{eff}} = 10.6 \mu_{\text{B}}/\text{Ho}$ and $\theta_{\text{CW}} = -14.3$ K, and low-temperature analysis yield $\theta_{\text{CW}} = -4.83$ K and $\mu_{\text{eff}} = 10.5 \mu_{\text{B}}/\text{Ho}^{3+}$. The obtained moment value is in accordance with the moment $10.60 \mu_{\text{B}}/\text{Ho}^{3+}$ of free Ho³⁺ (⁵I₈) ions. Considering that the Ho³⁺ ion in Ba₆Ho₂Ti₄O₁₇ share the same D_{3d} symmetry with the pyrochlore-lattice Ho₂Ti₂O₇ and triangular-lattice KBaHo(BO₃)₂ magnets,^{29,30} the formation of similar non-Kramers doublet with easy-axis (Ising) anisotropy is expected. The determination of CEF splitting using inelastic neutron spectroscopy (INS) will be required to clarify this issue. The $M(\mu_0 H)$ curve at 2 K exhibits maximum magnetization $M_{\text{S}} = 6.53 \mu_{\text{B}}/\text{Ho}$ at $\mu_0 H = 7$ T (Figure 4e), which is much smaller than $M_{\text{S}} = g_J \mu_{\text{B}} = 10 \mu_{\text{B}}/\text{Ho}^{3+}$ for free Ho³⁺ ions. At $T \geq 5$ K, the experimental $M(\mu_0 H)$ data can be well fitted by Brillouin function as expected for the paramagnetic state. In contrast, the Brillouin function fits deviate from the experimental data at 2 K, possibly due to the development of AFM interactions or the formation of non-Kramers doublet states at low temperatures.

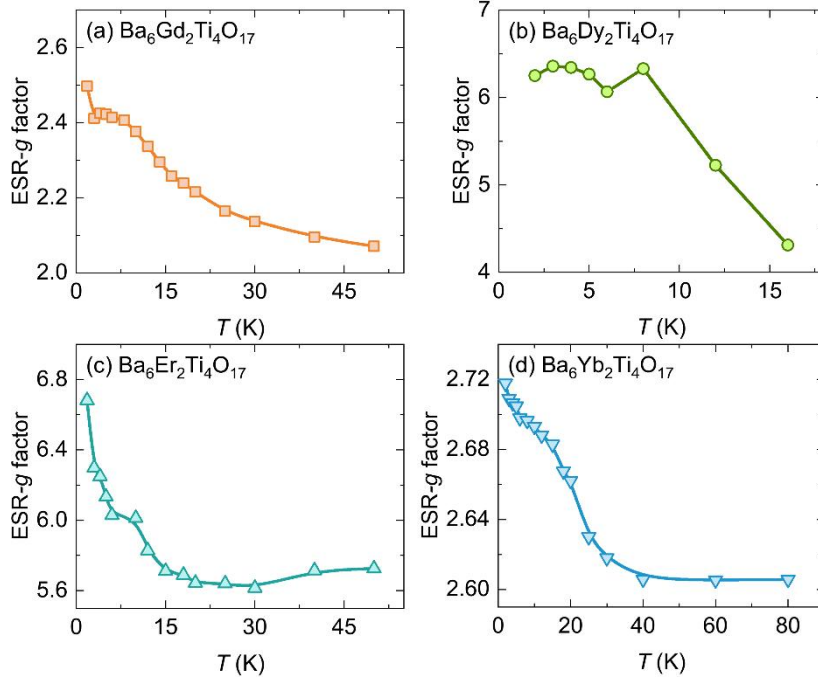


Figure 6. Temperature dependence of estimated ESR g -factors of $\text{Ba}_6\text{RE}_2\text{Ti}_4\text{O}_{17}$ compounds with (a) RE = Gd, (b) RE = Dy, (c) RE = Er, (d) RE = Yb.

$\text{Ba}_6\text{Er}_2\text{Ti}_4\text{O}_{17}$. The $\chi(T)$ curves of $\text{Ba}_6\text{Er}_2\text{Ti}_4\text{O}_{17}$ show no sign of magnetic transition down to 1.8 K, as shown in Figure 3f. At high-temperature regimes (120-300 K), the CW fits yield $\theta_{\text{CW}} = -9.46$ K and $\mu_{\text{eff}} = 9.53 \mu_{\text{B}}/\text{Er}$ close to the $9.59 \mu_{\text{B}}$ of free Er^{3+} ($4f^7$, $J=15/2$) ions. The low temperature fits give $\theta_{\text{CW}} = -2.08$ K and $\mu_{\text{eff}} = 8.30 \mu_{\text{B}}/\text{Er}$. This obtained θ_{CW} is smaller than the observation in ErMgGaO_4 but close to the θ_{CW} values in Er chalcogenides AErSe_2 ($\text{A} = \text{Na}^+, \text{K}^+$) and $\text{K}_3\text{Er}(\text{VO}_4)_2$.^{12,31,32} Figure 4f presents the isothermal $M(\mu_0H)$ curves at different temperatures for $\text{Ba}_6\text{Er}_2\text{Ti}_4\text{O}_{17}$, which exhibit a nonlinear relation at low fields and then increase linearly above 4 T with maximum magnetization $M_{\text{S}} \sim 5.65 \mu_{\text{B}}/\text{Er}$ at 7 T. From the ESR spectra shown in Figure 5c, single resonance lines are identified at different measured temperatures. As shown in Figure 6c the g -factor shows a steep increase from 5.72 to 6.68 as temperature decreases from 50 K to 2 K. If using the obtained g -factor $g_1=6.68$ and $J_{\text{eff}}=1/2$ at 2 K, the estimated magnetization $M_{\text{sat}} = gJ_{\text{eff}}\mu_{\text{B}} \sim 3.34\mu_{\text{B}}$ is much smaller the experimental value, which suggests the existence of magnetic contribution from the orbital moments of Er^{3+} ions.

$\text{Ba}_6\text{Tm}_2\text{Ti}_4\text{O}_{17}$. The magnetic susceptibility of $\text{Ba}_6\text{Tm}_2\text{Ti}_4\text{O}_{17}$ is shown in Figure 3g. As decreased temperatures, the $\chi(T)$ displays a broad hump at ~ 15 K, possibly related to the formation of two low-lying nonmagnetic singlet states for Tm^{3+} ($4f^{12}$) ions in the local D_{3d} symmetry environments analogous to the case of $\text{Ba}_9\text{Tm}_2(\text{SiO}_4)_6$ and TmMgGaO_4 compounds.^{21,33} High temperature CW fits give $\theta_{\text{CW}} = -25.7$ K and $\mu_{\text{eff}} = 7.71 \mu_{\text{B}}/\text{Tm}$, the moment value is close to the $\mu_{\text{eff}} = 7.57 \mu_{\text{B}}$ for Tm^{3+} free ions. At low temperatures, the isothermal magnetization $M(\mu_0H)$ curves don't show any sign of saturation to 7 T as shown in Figure 4g, this is also in accordance with the formation of two low-lying singlets state, which can give a Van Vleck magnetic contribution. At $T = 2$ K, the maximum magnetization value $\sim 1.4 \mu_{\text{B}}$ at $\mu_0H = 7$ T is far smaller than the

expected saturated magnetization $M_S = gJ\mu_B = 7\mu_B/\text{Tm}^{3+}$ for free Tm^{3+} ions.

Ba₆Yb₂Ti₄O₁₇. As shown in Figure 3h, high temperature CW fits on the $\chi^{-1}(T)$ of Ba₆Yb₂Ti₄O₁₇ give $\theta_{\text{CW}} = -112.6$ K and $\mu_{\text{eff}} = 4.86 \mu_B/\text{Yb}$, the moment is close to the value of free Yb^{3+} ion ($4.53 \mu_B$). The low temperature CW fits give $\theta_{\text{CW}} = -0.71$ K and $\mu_{\text{eff}} = 2.57 \mu_B/\text{Yb}$. The low-temperature fitted negative θ_{CW} indicates a dominant antiferromagnetic exchange interaction between Yb^{3+} moments. The $M(\mu_0H)$ curves at selected temperatures are shown in Figure 4h. After subtracting a linear dependent magnetization contribution (the slope of the linear fit for $H > 4$ T is $\chi_{\text{vV}} = 1.75 \times 10^{-2}$ emu/mol), the saturated moment is $\sim 1.28 \mu_B/\text{Yb}^{3+}$. This small magnetization supports the formation of doublet ground states described by $J_{\text{eff}} = 1/2$ effective moments. Also, the Brillouin function fitting yields a powder-average Landé g factor 2.67 at 2 K, this is in consistent with $g = 2.7$ evaluated from the single ESR spectra as shown in Figure 5d. The ESR g -factor increases dramatically as temperature decreases below 30 K (see Figure 6d). Using the obtained ESR g -factors at 2 K, the estimated effective magnetic moment $\mu_{\text{eff}} = g\sqrt{J(J+1)}\mu_B = 2.34 \mu_B$ is close to the experimental data.

For the compounds containing RE^{3+} ions, they can be divided into two categories: Kramers ions with odd $4f$ electrons (Nd^{3+} , Sm^{3+} , Dy^{3+} , Er^{3+} , and Yb^{3+}) and non-Kramers ions with even numbers of $4f$ electrons (Ho^{3+} , and Tm^{3+}). Among them, Gd^{3+} is special and has half-filled $4f$ shell ($4f^7$, $S=7/2$, $L=0$) with Heisenberg-like anisotropy and effective moment $S_{\text{eff}}=7/2$, then the negative value of $\theta_{\text{CW}} = -0.296$ K indicates the AFM interactions for Ba₆Gd₂Ti₄O₁₇. For the other compounds containing Kramers ions, low temperature magnetism can be well described by effective moment $J_{\text{eff}} = 1/2$ protected by time-reversal symmetry. While, for non-Kramers RE^{3+} ions, the situation is complicated and it can be taken as effective pseudospin $S_{\text{eff}} = 1/2$ state at low temperatures in case of the formation of a pair of low-lying CEF ground state singlet, which depends on the point group symmetry of REO_n coordinate environments. Here, the energy of magnetic interactions can be evaluated by the mean-field approximations of Ba₆RE₂Ti₄O₁₇, the superexchange interaction (J_{nn}) between localized RE^{3+} moments can be approximated by the relation,³⁴ $J_{\text{nn}} = (3k_B\theta_{\text{CW}})/zS(S+1)$, where S represents the effective spin quantum number and z is the number of nearest-neighbor spins (here $z = 6$). The dipolar interaction energy (D) can be estimated by $D = \mu_0\mu_{\text{eff}}^2/[4\pi(R_{\text{nn}})^3]$, where R_{nn} is the space separation between nearest-neighbor RE^{3+} ions within the triangular-lattice plane. Since the mean field approximations don't consider the local single-ion anisotropy of RE^{3+} ions and other contributions of exchange interaction, it only can give the rough estimation on the dipolar interaction and superexchange interaction in the energy scale, the accurate determination requires the inelastic neutron spectroscopy (INS) measurements on the Ba₆RE₂Ti₄O₁₇ compounds in the future. Moreover, the low-temperature fitted magnetic parameters θ_{CW} and μ_{eff} can relatively well reflect the magnetic interactions of ground state, then J_{nn} and D values are calculated using the low- T fitted θ_{CW} and μ_{eff} , as also provided in Table 3. From that, Ba₆Yb₂Ti₄O₁₇ as an example, the intralayers' exchange interaction and dipolar interaction is $D \sim 0.020$ K and $J_{\text{nn}} \sim -0.47$ K, and here the distance ratio for the Yb^{3+} ion between the interlayer and intralayer ones $\delta = d_1/d_0 \sim 1.25$, which is larger than ~ 1.17 for YbBO_3 compound.³⁵ Moreover, the estimated J/k_B (~ 0.47 K) in Ba₆Yb₂Ti₄O₁₇ is comparable to that of YbBO_3 (~ 0.53 K). As another typical feature, the "AA" type stacking fashion of layered triangular-lattice in Ba₆Yb₂Ti₄O₁₇ doesn't introduce the additional geometric frustration from the stacking order, this is different from the "ABC" stacking

fashion in NaBaYb(BO₃)₂ and NaYbS₂ compounds.^{36,37}

Table 3. The obtained magnetic parameters θ_{CW} and μ_{eff} from the Curie–Weiss fitting of $\chi(T)$ for Ba₆RE₂Ti₄O₁₇ (RE = Nd, Sm, Gd, Dy–Yb) samples and the effective moment μ_{fi} of free ions calculated by $g[J(J+1)]^{1/2}$, the calculated superexchange interaction (J_{nn}) and the in-plane dipolar interaction (D).

RE	High T fit	θ_{cw} (K)	μ_{eff} (μ_B)	Low T fit	θ_{cw} (K)	μ_{eff} (μ_B)	μ_{fi} (μ_B)	D (K)	J_{nn} (K) using J	J_{nn} (K) using $J_{eff} = 1/2$
Nd	120-300 K	-33.7	3.64	5-10 K	-1.74	2.50	3.62	0.018	-0.035	-1.16
Sm	–	–	–	5-10 K	-1.98	0.567	0.85	0.0009	-0.113	-1.32
Gd	120-300 K	-6.40	8.05	5-10 K	-0.276	7.69	7.94	0.173	-0.009	N/A
Dy	120-300 K	-13.3	10.4	5-10 K	-1.85	8.49	10.6	0.213	-0.015	-1.23
Ho	120-300 K	-14.3	10.6	5-10 K	-4.83	10.5	10.6	0.328	-0.034	-3.22
Er	120-300 K	-9.46	9.53	5-10 K	-2.08	8.30	9.59	0.205	-0.016	-1.39
Tm	120-300 K	-25.7	7.71	70-100 K	-34.2	7.92	7.57	0.188	-0.407	-22.8
Yb	120-300 K	-112.6	4.86	5-10 K	-0.71	2.57	4.53	0.020	-0.022	-0.47

Magnetic Property and Specific Heat of Ba₆Nd₂Ti₄O₁₇ Single Crystal.

Temperature dependence of magnetic susceptibilities of Ba₆Nd₂Ti₄O₁₇ single crystals were measured under field of $\mu_0H = 0.1$ T. Figure 7a shows the measured $\chi(T)$ curves for field along c -axis ($\mu_0H // c$) and perpendicular to c -axis ($\mu_0H // ab$ -plane), respectively. As shown in Figure 7b, high temperature fitted effective moments $\mu_{eff,ab} = 3.46 \mu_B/Nd$ ($\mu_0H // ab$) and $\mu_{eff,c} = 3.82 \mu_B/Nd$ ($\mu_0H // c$) are close to the value for free Nd³⁺ ion (3.62 μ_B). Using the magnetic susceptibilities of single crystals, the calculated average susceptibility ($\bar{\chi}$) of powders by $\bar{\chi} = \frac{1}{3}\chi_c + \frac{2}{3}\chi_{ab}$ agrees well with the experimental $\chi(T)$ data. For Ba₆Nd₂Ti₄O₁₇, the typical feature is that its magnetic susceptibilities exhibit the Ising-like anisotropy with easy magnetization along c -axis, the spin anisotropy (χ_c/χ_{ab}) reaches ~ 7.5 at 2 K. The low-temperature (2–4 K) fitted $\theta_{cw,c} = -0.19$ K and $\theta_{cw,ab} = -1.2$ K further support easy-axis anisotropy with dominant AFM exchange interactions, this is quite similar to the report in triangular-lattice NdTa₇O₁₉ with dominant Ising-like character,¹⁸ but different from the triangular-lattice TbInO₃ with an in-plane XY-type anisotropy.³⁸ The isothermal magnetization $M(\mu_0H)$ curves were measured at selected temperatures, the experimental results for $\mu_0H // c$ and $\mu_0H // ab$ are shown in Figure 7c, d, respectively. Along the c -axis, the magnetization reaches saturation with $M_S \sim 1.79 \mu_B/Nd$ at 7 T, which is close to 3 times larger than the value $\sim 0.64 \mu_B/Nd$ for $\mu_0H // ab$ -plane. To check the magnetic anisotropy, the ESR spectra were measured on Ba₆Nd₂Ti₄O₁₇ single crystals along the above two directions, the obtained ESR spectra at 2 K are shown in the inset of Figure 7e and 7f, respectively. We can identify two resolved ESR lines with peaks at μ_0H_{r1} and μ_0H_{r2} denoted by the dashed lines, which can be due to the hyperfine structure of ¹⁴³Nd ($I = 7/2$) and ¹⁴⁵Nd ($I = 7/2$) isotopes.^{39,40} Based on the ESR spectra shown in Figure S4, the temperature-dependent average Lande g -factors (g_{ave}) are shown in Figure 7e and Figure 7f. The values of $g_{ab} = 1.29$ ($\mu_0H // ab$) and $g_c = 3.49$ ($\mu_0H // c$) at 2 K support a strong Ising-like magnetic anisotropy.

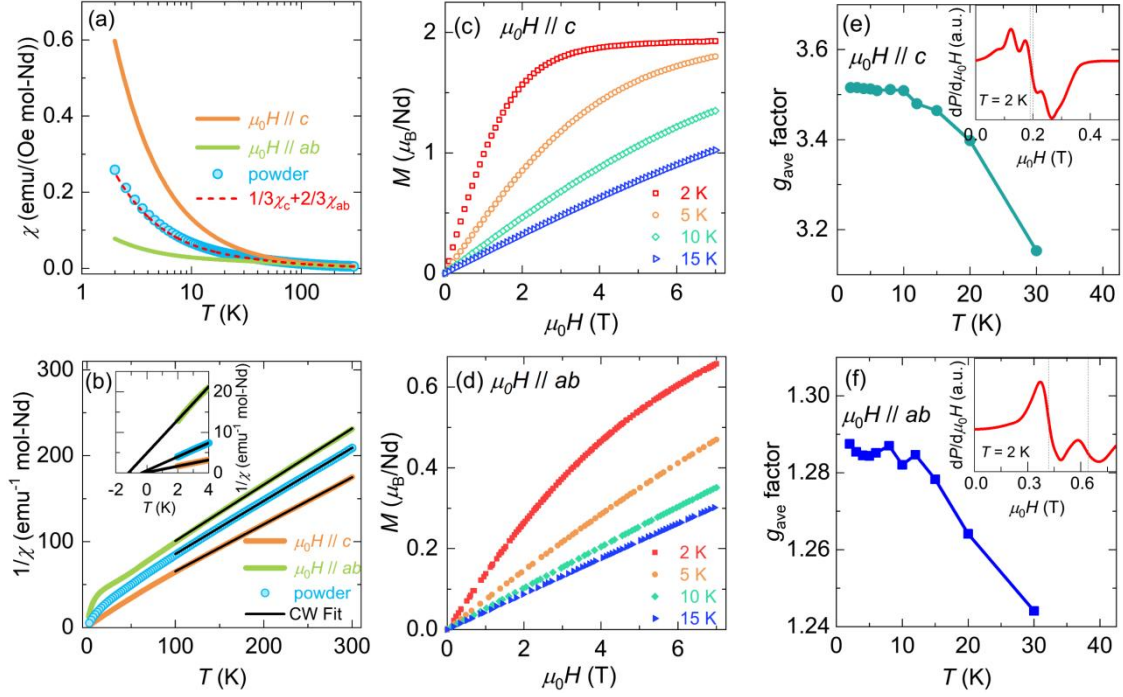


Figure 7. (a) Magnetic susceptibility (χ_c, χ_{ab}) of $\text{Ba}_6\text{Nd}_2\text{Ti}_4\text{O}_{17}$ single crystals for $\mu_0H // c$ -axis and $\mu_0H // ab$ -plane under field of 0.1 T, the susceptibility of polycrystals is also presented for comparison. The dashed red line shows the calculated magnetic susceptibility by $\bar{\chi} = \frac{1}{3}\chi_c + \frac{2}{3}\chi_{ab}$. (b) The Inverse susceptibility of $\text{Ba}_6\text{Nd}_2\text{Ti}_4\text{O}_{17}$ single crystals and its comparison with the ones of polycrystals, the black lines represent the CW fitted curves, the inset shows the low-temperature CW fitting analysis. (c, d) The isothermal $M(\mu_0H)$ curves of $\text{Ba}_6\text{Nd}_2\text{Ti}_4\text{O}_{17}$ single crystal for $\mu_0H // c$ -axis and $\mu_0H // ab$ -plane, respectively. (e, f) The temperature dependence of g -factors obtained from the ESR spectra of $\text{Ba}_6\text{Nd}_2\text{Ti}_4\text{O}_{17}$ single crystal for $\mu_0H // ab$ -plane and $\mu_0H // c$ -axis, the inset show the ESR spectra at 2 K.

To unveil the magnetic ground state, the specific heat $C_p(T)$ measurements were performed on the $\text{Ba}_6\text{Nd}_2\text{Ti}_4\text{O}_{17}$ single crystals at different magnetic fields with $\mu_0H // c$ -axis. Figure 8a shows the zero-field specific heat of $\text{Ba}_6\text{Nd}_2\text{Ti}_4\text{O}_{17}$. The zero-field $C_p(T)$ curves show a minimum at ~ 3 K then increase steeply down to the lowest measured temperatures. No any sharp peak is detected, ruling out the magnetic transition with temperature down to ~ 0.08 K. After subtracting the lattice contribution using the isostructural nonmagnetic $\text{Ba}_6\text{Eu}_2\text{Ti}_4\text{O}_{17}$ as the reference, temperature dependence of magnetic heat capacity $C_{\text{mag}}(T) = C_p(T) - C_{\text{Latt}}(T)$ is shown in Figure 8b. Under applied field, the $C_{\text{mag}}(T)$ curves don't show any sharp peak at $T \geq 0.1$ K indicating the absence of field-induced long-range magnetic order. For $\mu_0H \geq 0.5$ T, the $C_{\text{mag}}(T)$ curves show a broad maximum and shift to higher temperatures. The height of the peaks with the same amplitude as $\mu_0H \geq 1$ T reveals a Schottky-like anomaly. Further integrating the $C_{\text{mag}}(T)/T$ with respect to temperature, the changes of magnetic entropy (ΔS_{mag}) at different fields are plotted on Figure 8c. As seen, the calculated magnetic entropy

from 0.08 K to 15 K approaches $R\ln 2$ for $\mu_0 H \geq 1$ T, this is expected for the formation of $J_{\text{eff}} = 1/2$ Kramers doublet ground state. While the zero-field release of ΔS_{mag} only reaches $\sim 0.27R\ln 2$, leaving $\sim 73\%$ of entropy at temperatures below 0.08 K.

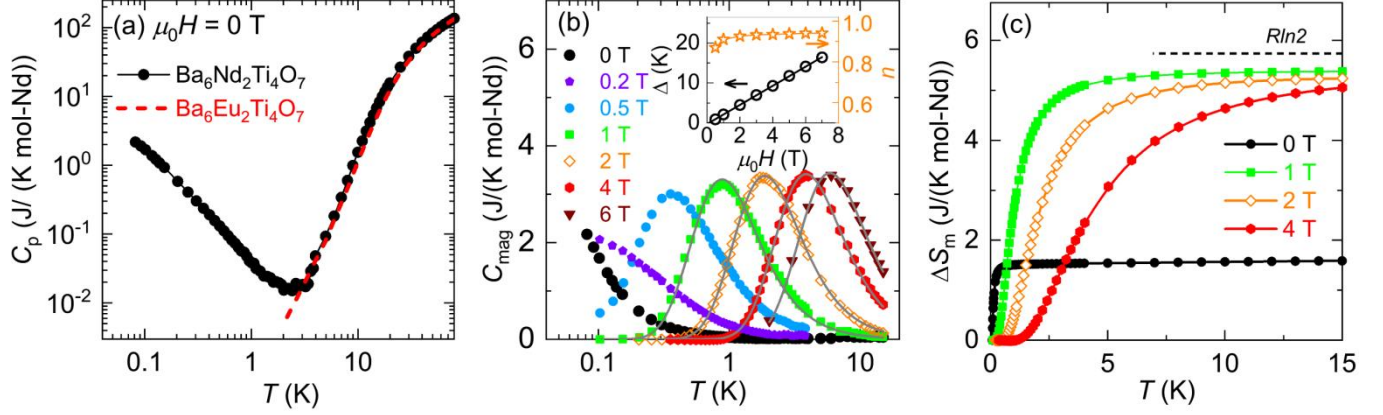


Figure 8. (a) Temperature dependence of zero-field specific heat $C_p(T)$ curves of $\text{Ba}_6\text{Nd}_2\text{Ti}_4\text{O}_{17}$ single crystal and $\text{Ba}_6\text{Eu}_2\text{Ti}_4\text{O}_{17}$ polycrystals. (b) Temperature dependence of magnetic specific heat $C_{\text{mag}}(T)$ of $\text{Ba}_6\text{Nd}_2\text{Ti}_4\text{O}_{17}$ single crystal at different fields for field along c -axis, the gray lines represent the fits by the two-level Schottky function, inset shows the energy gap Δ and the concentration n versus $\mu_0 H$. (c) Magnetic entropy $\Delta S_m(T)$ of $\text{Ba}_6\text{Nd}_2\text{Ti}_4\text{O}_{17}$ under different fields.

Using the two-level Schottky function (C_{sch}), $C_{\text{mag}}(T)$ curves are fitted by the following relation: $C_{\text{sch}} = nR\left(\frac{\Delta}{T}\right)^2 \frac{\exp(\Delta/T)}{[1+\exp(\Delta/T)]^2}$, where n is the concentration of Schottky centers, and R is an ideal gas constant, and Δ is the Zeeman energy gap between two levels.¹⁶ The fitted curves are denoted by the solid gray lines in Figure 8b. From the above fitting, the crystal field energy gap Δ increases linearly versus $\mu_0 H$ (see the inset of Figure 8b), and the zero-field energy gap Δ is close to zero, the fitted $n \approx 1$ for $\mu_0 H \geq 2$ T indicates the Nd^{3+} spins are excited to the higher-energy levels in the two levels. As shown in Figure 8c, the released magnetic entropy $S_m(T)$ under $\mu_0 H = 4$ T reaches a saturation value $\sim R\ln 2$ in accordance with the doublet ground state. No further increase of $S_m(T)$ indicates a well separation for the first CEF excited level from the doublet ground state with a large energy gap. Thus, it can be well considered as an effective $J_{\text{eff}}=1/2$ system at low temperatures. The presence of magnetic frustration with frustration index $f = |\theta_{\text{CW}}/T_N|$ of 2.4~15 as well as its absence of long-range magnetic order down to 0.08 K. Compared to the lack of magnetic characterization of single crystal form on $\text{NdTa}_7\text{O}_{19}$ as Ising triangular-lattice QSL candidate,¹⁸ here the successful growth of $\text{Ba}_6\text{Nd}_2\text{Ti}_4\text{O}_{17}$ single crystal allow us to establish its magnetic ground state and anisotropic magnetic behaviors.

■ CONCLUSIONS

A new family of rare-earth-based triangular lattice magnets, $\text{Ba}_6\text{RE}_2\text{Ti}_4\text{O}_{17}$ (RE = Nd, Sm, Gd, Dy–Ho), were successfully synthesized and magnetically characterized, where the layered magnetic triangular lattice planes are stacked in an eclipsed “AA”-type stacking fashion along the c -axis. Structural analysis reveals that

these compounds are free of chemical antisite occupancy between the RE and Ba/Ti cations, making them attractive for studying the intrinsic triangular lattice physics. All $\text{Ba}_6\text{RE}_2\text{Ti}_4\text{O}_{17}$ compounds display dominant antiferromagnetic interactions between the RE^{3+} moments without magnetic transition down to 1.8 K. The analyses of isothermal magnetizations reveal the presence of different magnetic anisotropy for different RE ions. More importantly, the synthesized $\text{Ba}_6\text{Nd}_2\text{Ti}_4\text{O}_{17}$ single crystals exhibit a strong Ising-like anisotropy along *c*-axis and absence of long-range magnetic order down to 0.08 K, being an Ising-type quantum magnet with effective $J_{\text{eff}}=1/2$ local moment.

■ Accession Codes

CCDC 2306558 contains the supplementary crystallographic data for this paper. This data can be obtained free of charge via http://www.ccdc.cam.ac.uk/data_request/cif, or emailing data_request@ccdc.cam.ac.uk.

■ AUTHOR INFORMATION

Corresponding Author

Hanjie Guo –Songshan Lake Materials Laboratory, Dongguan, Guangdong 523808, P. R. China; orcid.org/0000-0001-6203-5557; Email: hjguo@sslslab.org.cn

Zhaoming Tian – School of Physics and Wuhan National High Magnetic Field Center, Huazhong University of Science and Technology, Wuhan 430074, PR China. orcid.org/0000-0001-6538-3311; Email: tianzhaoming@hust.edu.cn.

Authors

Fangyuan Song–School of Physics and Wuhan National High Magnetic Field Center, Huazhong University of Science and Technology, Wuhan, 430074, P. R. China

Andi Liu–School of Physics and Wuhan National High Magnetic Field Center, Huazhong University of Science and Technology, Wuhan, 430074, P. R. China; Songshan Lake Materials Laboratory, Dongguan, Guangdong 523808, P. R. China

Qiao Chen–School of Physics and MOE Key Laboratory of Fundamental Physical quantum Physics, PGMF, Huazhong University of Science and Technology, Wuhan 430074, China

Jin Zhou–School of Physics and Wuhan National High Magnetic Field Center, Huazhong University of Science and Technology, Wuhan, 430074, P. R. China

Jingxin Li–Anhui Province Key Laboratory of Condensed Matter Physics at Extreme Conditions, High Magnetic Field Laboratory, HFIPS, Chinese Academy of Sciences, Hefei, Anhui 230031, P. R. China

Wei Tong –Anhui Province Key Laboratory of Condensed Matter Physics at Extreme Conditions, High Magnetic Field Laboratory, HFIPS, Chinese Academy of Sciences, Hefei, Anhui 230031, P.R. China

Shun Wang–School of Physics and MOE Key Laboratory of Fundamental Physical quantum Physics, PGMF, Huazhong University of Science and Technology, Wuhan 430074, China

Yanhong, Wang–Key Laboratory of Material Chemistry for Energy Conversion and Storage, School of Chemistry and Chemical Engineering, Huazhong University of Science and Technology, Wuhan, 430074, China.

Hongcheng Lu—Key Laboratory of Material Chemistry for Energy Conversion and Storage, School of Chemistry and Chemical Engineering, Huazhong University of Science and Technology, Wuhan, 430074, China.

Songliu Yuan—School of Physics, Huazhong University of Science and Technology, Wuhan 430074, PR China

■ ASSOCIATED CONTENT

Supporting Information

The crystal structure parameters of $\text{Ba}_6\text{RE}_2\text{Ti}_4\text{O}_{17}$ polycrystals, low-temperature magnetic parameters and X-band ESR spectra of $\text{Ba}_6\text{Nd}_2\text{Ti}_4\text{O}_{17}$ single crystal. (PDF)

■ ACKNOWLEDGEMENTS

This work was supported by the National Natural Science Foundation of China (Grant No. 11874158), the Fundamental Research Funds of Guangdong Province (Grant No. 2022A1515010658) and Guangdong Basic and Applied Basic Research Foundation (Grant No.2022B1515120020). This work was supported by the synergetic extreme condition user facility (SECUF), and a portion of magnetic measurement was performed on the Steady High Magnetic Field Facilities, High Magnetic Field Laboratory. We would like to thank Guifen Ren for her assistance on the specific heat measurement and thank the staff of the analysis center of Huazhong University of Science and Technology for their assistance in structural characterizations.

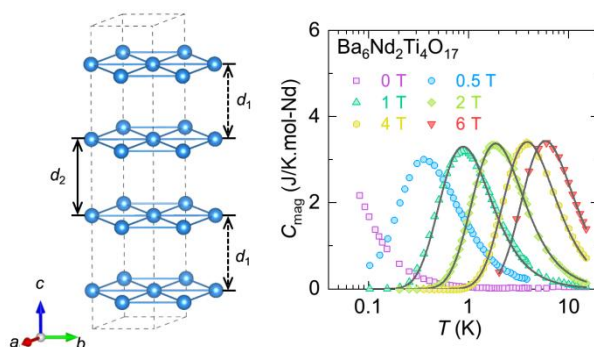
■ REFERENCES

- (1) Anderson, P.W. Resonating valence bonds: A new kind of insulator? *Mater. Res. Bull.* **1973**, *8*, 153.
- (2) Shimizu, Y.; Miyagawa, K.; Kanoda, K.; Maesato, M.; Saito, G. Spin-liquid state in an organic mott insulator with a triangular lattice. *Phys. Rev. Lett.* **2003**, *91*, 107001.
- (3) Itou, T.; Oyamada, A.; Maegawa, S.; Tamura, M.; R. Kato. Quantum spin liquid in the spin-1/2 triangular antiferromagnet $\text{EtMe}_2\text{Sb}[\text{Pd}(\text{dmit})_2]_2$. *Phys. Rev. B* **2008**, *77*, 104413.
- (4) Nakatsuj, S.; Nambu, Y.; Tonomura, H.; Sakai, O.; Jonas, S.; Broholm, C.; Tsunetsugu, H.; Qiu, Y.; Maeno, Y. Spin disorder on a triangular lattice. *Science* **2005**, *309*, 1697.
- (5) Zhou, H. D.; Choi, E. S.; Li, G.; Balicas, L.; Wiebe, C. R.; Qiu, Y.; Copley, J. R. D.; Gardner, J. S. Spin Liquid State in the $S = 1/2$ Triangular Lattice $\text{Ba}_3\text{CuSb}_2\text{O}_9$. *Phys. Rev. Lett.* **2011**, *106*, 147204.
- (6) Ono, T.; Tanaka, H.; Aruga Katori, H.; Ishikawa, F.; Mitamura, H.; Goto, T. Magnetization plateau in the frustrated quantum spin system Cs_2CuBr_4 . *Phys. Rev. B* **2023**, *67*, 104431.
- (7) Sheng, J.; Wang, L.; Candini, A.; Jiang, W.; Huang, L.; Xi, B.; Zhao, J.; Ge, H.; Zhao, N.; Fu, Y. Ren, J. Yang, J.; Miao, P. Tong, X.; Yu, D.; Wang, S. Liu, Q.; Maiko, K.; Mole, R.; Biasiol, G.; Yu, D.; Zaliznyak, Igor A.; Mei, J.W.; Wu, L. Two-dimensional quantum universality in the spin-1/2 triangular-lattice quantum antiferromagnet $\text{Na}_2\text{BaCo}(\text{PO}_4)_2$. *PNAS*, **2022**, *119*, e2211193119.
- (8) Li, Y.; Chen, G.; Tong, W.; Pi, L.; Liu, J.; Yang, Z.; Wang, X.; Zhang, Q. Rare-earth triangular lattice spin liquid: a single-crystal study of YbMgGaO_4 . *Phys. Rev. Lett.* **2015**, *115*, 167203.
- (9) Liu, W.; Zhang, Z.; Ji, J.; Liu, Y.; Li, J.; Wang, X.; Lei, H.; Chen, G.; Zhang, Q. Rare-Earth Chalcogenides: A Large Family of Triangular Lattice Spin Liquid Candidates. *Chin. Phys. Lett.* **2018**, *35*, 117501.
- (10) Dissanayaka Mudiyansele, R. S.; Wang, H.; Vilella, O.; Mourigal, M.; Kotliar, G.; and Xie, W. LiYbSe_2 : Frustrated Magnetism in the Pyrochlore Lattice. *J. Am. Chem. Soc.* **2022**, *144*, 11933–11937.
- (11) Ashtar, M.; Gao, Y. X.; Wang, C. L.; Qiu, Y.; Tong, W.; Zou, Y. M.; Zhang, X. W.; Marwat, M. A.; Yuan, S. L.; Tian, Z. M.

- Synthesis, structure and magnetic properties of rare-earth $\text{RE}\text{MgAl}_{11}\text{O}_{19}$ ($\text{RE}=\text{Pr},\text{Nd}$) compounds with two-dimensional triangular lattice. *J. Alloys Compd.* **2019**, *802*, 146–151.
- (12) Xing, Jie.; Sanjeeva, L. D.; Kim, J.; Meier, W. R.; May, A. F.; Zheng, Q.; Custelcean, R.; Stewart, G. R.; Sefat, A. S. Synthesis, magnetization, and heat capacity of triangular lattice materials NaErSe_2 and KErSe_2 . *Phys. Rev. Materials* **2019**, *3*, 114413.
- (13) Bu, H.; Ashtar, M.; Shiroka, T.; Walker, H. C.; Fu, Z.; Zhao, J.; Gardner, J. S.; Chen, G.; Tian, Z.; Guo, H. Gapless triangular-lattice spin-liquid candidate $\text{PrZnAl}_{11}\text{O}_{19}$. *Phys. Rev. B* **2022**, *106*, 134428.
- (14) Hu, Z.; Ma, Z.; Liao, Y. D.; Li, H.; Ma, C.; Cui, Y.; Shangguan, Y.; Huang, Z.; Qi, Y.; Li, W.; Meng, Z. Y. Wen J. Yu, W. Evidence of the Berezinskii-Kosterlitz-Thouless phase in a frustrated magnet. *Nat. Commun.* **2020**, *11*, 5631.
- (15) Ma, Z.; Wang, J.; Dong, Z. Y.; Zhang, J.; Li, S.; Zheng, S. H.; Yu, Y.; Wang, W.; Che, L.; Ran, K.; Bao, S.; Cai, Z.; Čermák, P.; Schneidewind, A.; Yano, S.; Gardne, J. S.; Lu, X.; Yu, S.L.; Liu, J.M.; Li, S.; Li, J. X.; Wen, J. Spin-Glass Ground State in a Triangular-Lattice Compound YbZnGaO_4 . *Phys. Rev. Lett.* **2018**, *120*, 087201.
- (16) Bag, R.; Ennis, M.; Liu, C.; Dissanayake, S. E.; Shi, Z.; Liu, J.; Balents, L.; Haravifard, S. Realization of quantum dipoles in triangular lattice crystal $\text{Ba}_3\text{Yb}(\text{BO}_3)_3$. *Phys. Rev. B* **2021**, *104*, L220403.
- (17) Wen, J.; Yu, S.L. Li, S.; Yu, W.; Li, J. X. Experimental identification of quantum spin liquids. *NPJ. Quantum Mater.* **2019**, *4*, 12.
- (18) Arh, T.; Sana, B.; Pregelj, M.; Khuntia, P.; Jagličić, Z.; Le, M. D.; Biswas, P. K.; Manuel, P.; Mangin-Thro, L.; Ozarowski, A.; Zorko, A. The Ising triangular-lattice antiferromagnet neodymium heptatantalate as a quantum spin liquid candidate. *Nat. Mater.* **2022**, *21*, 416–422.
- (19) Liu, J.; Yao, X. P.; Chen, G. Stacking-induced magnetic frustration and spiral spin liquid. *Phys. Rev. B* **2022**, *106*, L220410.
- (20) Hikihara, T.; Misawa, T.; Momoi, T. Spin nematics in frustrated spin-dimer systems with bilayer structure. *Phys. Rev. B* **2019**, *100*, 214414.
- (21) Kuang, X.; Jing, X.; Loong, C. K.; E. E.; Skakle, J. M. S.; West, A. R. A New Hexagonal 12-Layer Perovskite-Related Structure: $\text{Ba}_6\text{R}_2\text{Ti}_4\text{O}_{17}$ ($\text{R} = \text{Nd}$ and Y). *Chem. Mater.* **2002**, *14*, 4359-4363.
- (22) Liu, A.; Song, F.; Bu, H.; Li, Z.; Ashtar, M.; Qin, Y.; Liu, D.; Xia, Z.; Li, J.; Zhang, Z.; Tong, W.; Guo, H.; Tian Z. $\text{Ba}_9\text{RE}_2(\text{SiO}_4)_6$ ($\text{RE} = \text{Ho}-\text{Yb}$): A Family of Rare-Earth-Based Honeycomb-Lattice Magnets. *Inorg. Chem.* **2023**, *62*, 13867–13876.
- (23) Sanjeeva, L. D.; Xing, J.; Taddei, K. M.; Sefat, A. S. Synthesis, crystal structure and magnetic properties of KLnSe_2 ($\text{Ln}=\text{La}, \text{Ce}, \text{Pr}, \text{Nd}$) structures: A family of 2D triangular lattice frustrated magnets. *J. Solid State Chem.* **2022**, *308*, 122917.
- (24) Ranjith, K. M.; Dmytriieva, D.; Khim, S.; Sichelschmidt, J.; Luther, S.; Ehlers, D.; Yasuoka, H.; J. Wosnitzer, J.; Tsirlin, A. A.; Kühne, H.; Baenitz, M. Field-induced instability of the quantum spin liquid ground state in the $J_{\text{eff}} = 1/2$ triangular-lattice compound NaYbO_2 . *Phys. Rev. B* **2019**, *99*, 180401(R).
- (25) Xu, J.; Anand, V. K.; Bera, A. K.; Frontzek, M.; Abernathy, D. L.; Casati, N.; Siemensmeyer, K.; Lake, B. Investigation of the magnetic structure and crystal field states of pyrochlore antiferromagnet $\text{Nd}_2\text{Zr}_2\text{O}_7$. *Phys. Rev. B: Condens. Matter Mater. Phys.* **2015**, *92*, 224430.
- (26) Sanders, M. B.; Krizan, J. W.; Cava, R. J. $\text{RE}_3\text{Sb}_3\text{Zn}_2\text{O}_{14}$ ($\text{RE} = \text{La}, \text{Nd}, \text{Sm}, \text{Eu}, \text{Gd}$): a new family of pyrochlore derivatives with rare earth ions on a 2D Kagomé lattice. *J. Mater. Chem. C* **2016**, *4*, 541.
- (27) Ashtar, M.; Guo J.; Wan, Z.; Wang, Y.; Gong, G.; Liu, Y.; Su Y.; Tian, Z. A New Family of Disorder-Free Rare-Earth-Based Kagome Lattice Magnets: Structure and Magnetic Characterizations of RE_3BWO_9 ($\text{RE} = \text{Nd}, \text{Gd}-\text{Ho}$) Boratotungstates. *Inorg. Chem.* **2020**, *59*, 5368–5376.
- (28) Singh, S.; Saha, S.; Dhar, S. K.; Suryanarayanan, R.; Sood, A. K.; Revcolevschi, A. Manifestation of geometric frustration on magnetic and thermodynamic properties of the pyrochlores $\text{Sm}_2\text{X}_2\text{O}_7$ ($\text{X} = \text{Ti}, \text{Zr}$). *Phys. Rev. B: Condens. Matter Mater. Phys.* **2008**, *77*, 054408.

- (29) Petrenko, O. A.; Lees, M. R.; Balakrishnan, G. Magnetization process in the spin-ice compound $\text{Ho}_2\text{Ti}_2\text{O}_7$. *Phys. Rev. B* **2003**, *68*, 012406.
- (30) Guo, S.; Kong, T.; Alex Cevallos, F.; Stolze, K.; Cava, R. J. Crystal growth, crystal structure and anisotropic magnetic properties of $\text{KBaR}(\text{BO}_3)_2$ ($\text{R}=\text{Y, Gd, Tb, Dy, Ho, Tm, Yb}$ and Lu) triangular lattice materials. *J. Magn. Magn. Mater.* **2019**, *472*, 104–110.
- (31) Cai, Y.; Lygouras, C.; Thomas, G.; Wilson, M. N.; Beare, J.; Sharma, S.; Marjerrison, C. A.; Yahne, D. R.; Ross, K. A.; Gong, Z.; Uemura, Y.J.; Dabkowska, H.A.; Luke, G.M. μSR study of the triangular Ising antiferromagnet ErMgGaO_4 . *Phys. Rev. B* **2020**, *101*, 094432.
- (32) Yahne, D. R.; Sanjeewa, L. D.; Sefat, A. S.; Stadelman, B. S.; Kolis, J. W.; Calder, S.; Ross, K. A. Pseudospin versus magnetic dipole moment ordering in the isosceles triangular lattice material $\text{K}_3\text{Er}(\text{VO}_4)_2$. *Phys. Rev. B* **2020**, *102*, 104423.
- (33) Liu, C.; Huang, C. J.; Chen, G. Intrinsic quantum Ising model on a triangular lattice magnet TmMgGaO_4 . *Phys. Rev. Res.* **2020**, *2*, 043013.
- (34) Ramirez, A. P. Strongly geometrically frustrated magnets. *Annu. Rev. Mater. Sci.* **1994**, *24*, 453-480.
- (35) Somesh, K.; Islam, S. S.; Mohanty, S.; Simutis, G.; Guguchia, Z.; Wang, Ch.; Sichelschmidt, J.; Baenitz, M.; Nath, R. Absence of magnetic order and emergence of unconventional fluctuations in the $J_{\text{eff}} = 1/2$ triangular-lattice antiferromagnet YbBO_3 . *Phys. Rev. B* **2023**, *107*, 064421.
- (36) Guo, S.; Ghasemi, A.; Broholm, C. L.; Cava, R. J. Magnetism on ideal triangular lattices in $\text{NaBaYb}(\text{BO}_3)_2$. *Phys. Rev. Mater.* **2019**, *3*, 094404.
- (37) Baenitz, M.; Schlender, Ph.; Sichelschmidt, J.; Onykienko, Y. A.; Zangeneh, Z.; Ranjith, K. M.; Sarkar, R.; Hozoi, L.; Walker, H. C.; Orain, J. C.; Yasuoka, H.; van den Brink, J.; Klauss, H. H.; Inosov, D. S.; Doert, Th. NaYbS_2 : A planar spin-1/2 triangular-lattice magnet and putative spin liquid. *Phys. Rev. B* **2018**, *98*, 220409(R).
- (38) Clark, L.; Sala, G.; Maharaj, D. D.; Stone, M. B.; Knight, K. S.; Telling, M. T. F.; Wang, X.; Xu, X.; Kim, J.; Li, Y.; Cheong, S. W.; Gaulin, B. D. Two-dimensional spin liquid behaviour in the triangular-honeycomb antiferromagnet TbInO_3 . *Nat. Phys.* **2019**, *15*, 262–268.
- (39) Schulz, M. B.; Jeffries, C. D. Spin-lattice relaxation of rare-earth ions in LaF_3 . *Phys. Rev.* **1966**, *149*, 270-289.
- (40) Misra, S. K.; Isber, S. EPR of the Kramers ions Er^{3+} , Nd^{3+} , Yb^{3+} and Ce^{3+} in $\text{Y}(\text{NO}_3)_3 \cdot 6\text{H}_2\text{O}$ and $\text{Y}_2(\text{SO}_4)_3 \cdot 8\text{H}_2\text{O}$ single crystals: Study of hyperfine transitions. *Physica B* **1998**, *253*, 111-122.

For Table of Contents Only



Synopsis

The triangular-lattice magnet $\text{Ba}_6\text{Nd}_2\text{Ti}_4\text{O}_{17}$ crystallizes into the hexagonal structure with space group $P6_3/mmc$, where the magnetic Nd^{3+} ions locate on the layered triangular lattice planes within the ab -plane and are stacked in an "AA"-type fashion along the c -axis. The low-temperature specific heat results show that no long-range magnetic ordering is detected down to 0.08 K.